LOWER BOUNDS ON ASTROMETRIC ERRORS FROM A SPINNING, PRECESSING ASTROMETRIC SATELLITE DUE TO THE GEOMETRY OF THE OBSERVATION SCANNING PATTERN

Marc A. Murison
U.S. Naval Observatory, 3450 Massachusetts Ave NW, Washington DC 20392
murison@usno.navy.mil

April 19, 2001   D:\FAME\dynamics\ObservationDensity\DDA_2001.lwp

ABSTRACT

The scanning pattern of observations from a spin-stabilized, precessing astrometric spacecraft constrains the mission astrometric errors through the geometry that determines two distributions on the sky: the distribution of observation density and the distribution of scan angle (the angle of scan direction with respect to an ecliptic meridian through a given location). In this paper, the geometry underlying the distributions is presented. Then, assuming a given single-measurement error, simulated astrometric observations are accumulated on an equal-area grid on the sky. The behaviors of the astrometric error distributions are investigated as functions of the geometry control parameters: spin period, precession period, and precession cone angle (nominal angle between spin axis and Sun direction). Optimal values are determined for the specific case of the NASA MIDEX mission, FAME.

Key words: space astrometry — astrometric error — FAME

1. WHAT IS A SCANNING ASTROMETRIC SPACE-CRAFT?

▶ Space-based platform for making precise astrometric measurements (e.g., Hipparcos, FAME).

▶ Platform is spin-stabilized (and therefore much less expensive).

▶ Telescope(s) point orthogonal to the spin axis, scanning a strip of the sky one field of view (FOV) in width over the course of one spin period (tens of minutes).

▶ Precession of the spin axis (around, say, the Sun direction) produces a wide, spirograph-like scan pattern on the sky whose width is twice the precession cone angle ψ. See Figure 1. The precession period (days) is much longer than the spin period.

▶ Earth orbital motion causes the spirograph-like scan pattern to slowly rotate (rotation axis through the ecliptic poles), producing full-sky coverage.

▶ **This basic scanning geometry will have a fundamental impact on mission-averaged astrometric accuracies.**

2. WHAT DETERMINES MISSION ACCURACIES?

▶ Broadly speaking, we have "global" and "local" effects to consider regarding mission-averaged astrometric accuracies (see Figure 2).

▶ Local

  • instrumental parameters and characteristics

  • detailed spin and orbit dynamical motions

  • this category contains all the physics

  • determines single-measurement accuracies

▶ Global

  • driven entirely by the scanning geometry

  • constrains **two fundamental distributions**

◆ **distribution of observation density** (a function of position on the sky)

◆ **distribution of scan angles** (also a function of sky position)

  ▫ **scan angle:** at a given point on the sky, the angle that the telescope FOV motion makes with respect to an ecliptic meridian through that point.

• Sets upper bounds on the mission-averaged accuracies that the instrument can achieve, given

  ◆ the instrument geometry and

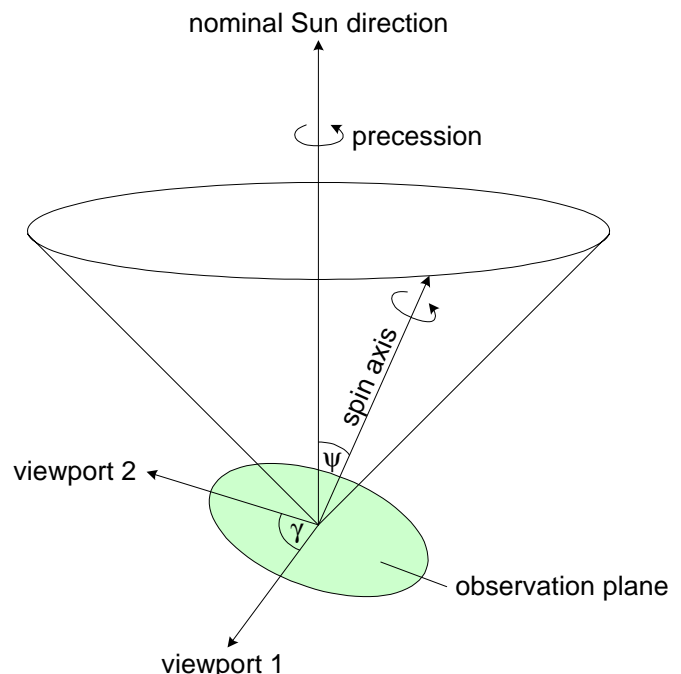 ◆ a statistical description of the single-measurement errors.

Figure 1 — Scanning motions of a scanning astrometric satellite with two telescope viewports.
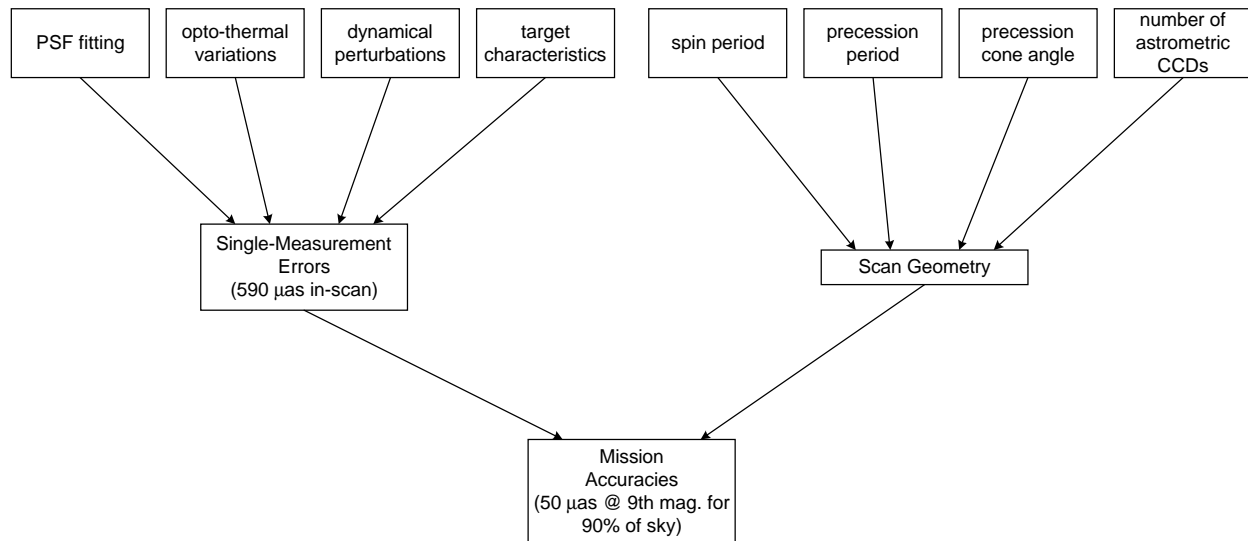
Figure 2 — Mission errors are determined by (1) single-measurement errors, a local effect, and (2) the scan geometry, a global constraint. Numbers given are for FAME.

▸ **This paper is concerned with the constraints on mission accuracies produced by the scanning geometry.**

3. GEOMETRY

Some basic geometry appropriate to the problem. First we relate a spacecraft "body frame" $[x, y, z]$, which is fixed to and spins along with the spacecraft, to an "external frame" $[X, Y, Z]$, with linkage provided by a convenient set of Euler angles. See Figure 3 for an illustration and definitions. The external frame need not be inertial. From this, one can construct the spherical triangles illustrated in Figure 4.

▸ The Euler angles are functions of time, derived from (and specified by) the spacecraft rigid body dynamics. We will assume these functions are given.

▸ Ecliptic coordinates of the viewports, as a function of the Euler angles (and therefore time):

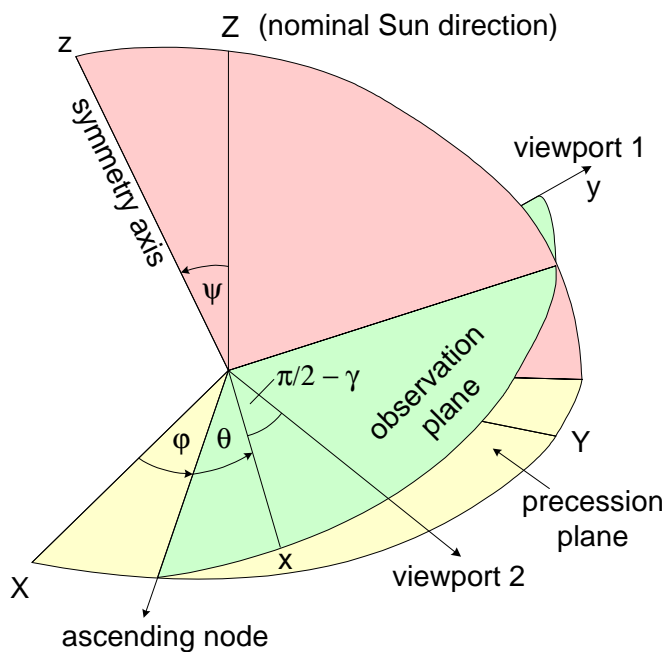$$\sin\beta = -\sin\varphi\sin\theta + \cos\varphi\cos\theta\cos\psi$$

Figure 3 — The body frame $[x, y, z]$ and the external frame $[X, Y, Z]$, connected by the Euler angles $[\theta, \psi, \varphi]$. The "fast" angle, or spin phase, is θ; the precession phase is φ; and the precession cone angle, or nominal Sun angle, is ψ. Two telescope viewports, whose directions define an "observation plane", are separated by the "basic angle", γ. Viewport 1 points along the body y axis.
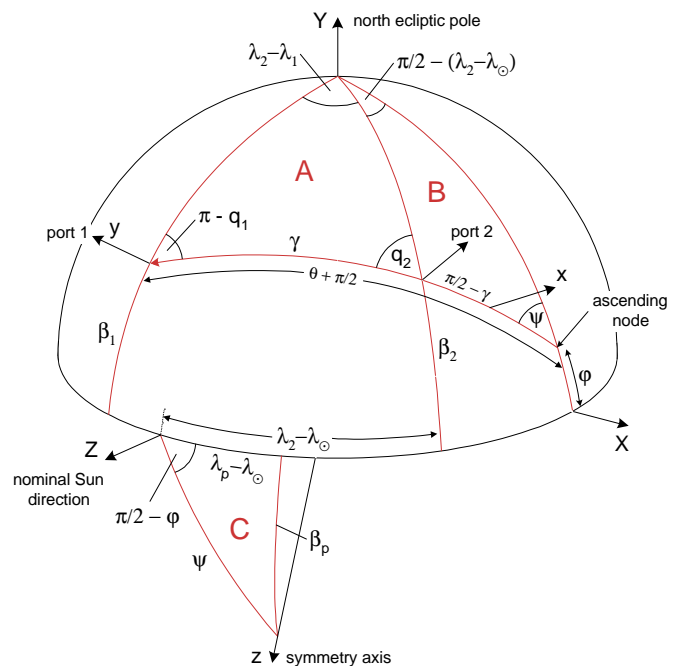
Figure 4 — Spherical geometry of the two viewports and the symmetry axis spin vector, in the ecliptic coordinate frame.

$$\cos\lambda = \frac{\cos\theta\sin\psi\cos\lambda_\odot + (\sin\theta\cos\varphi + \cos\theta\sin\varphi\cos\psi)\sin\lambda_\odot}{\sqrt{1 - (\cos\varphi\cos\theta\cos\psi - \sin\varphi\sin\theta)^2}}$$

$$\sin\lambda = \frac{\cos\theta\sin\psi\sin\lambda_\odot - (\sin\theta\cos\varphi + \cos\theta\sin\varphi\cos\psi)\cos\lambda_\odot}{\sqrt{1 - (\cos\varphi\cos\theta\cos\psi - \sin\varphi\sin\theta)^2}}$$

where $\lambda_\odot$ is the ecliptic longitude of the Sun. For viewport 2 (the trailing viewport), substitute $\theta - \gamma$ for θ.

▸ Using these, one can numerically build up the distribution of observations on the sky.

▸ The scan angle is

$$\cos q = -\frac{(\cos\phi\cos\theta\cos\psi - \sin\phi\sin\theta)\sin\theta + \sin\phi}{\sqrt{1 - (\cos\phi\cos\theta\cos\psi - \sin\phi\sin\theta)^2}\ \sin\theta}$$

$$\sin q = \frac{\cos\phi\sin\psi}{\sqrt{1 - (\cos\phi\cos\theta\cos\psi - \sin\phi\sin\theta)^2}}$$

▸ One can also obtain from the geometry the scan angle as a function of ecliptic coordinates:

$$\sin q = Q$$

$$\cos q = \frac{[\sin^2(\lambda - \lambda_\odot) - \cos^2(\lambda - \lambda_\odot)\sin^2\beta]\cos\psi}{\sin(\lambda - \lambda_\odot)[1 - \cos^2(\lambda - \lambda_\odot)\cos^2\beta]}$$

$$+ \frac{[\cos^2(\lambda - \lambda_\odot) - \sin^2\psi]\cos(\lambda - \lambda_\odot)\sin\beta}{Q\sin(\lambda - \lambda_\odot)[1 - \cos^2(\lambda - \lambda_\odot)\cos^2\beta]}$$

where Q is the pair of quadratic solutions

$$Q = \frac{\cos(\lambda - \lambda_\odot)\cos\psi\sin\beta}{1 - \cos^2(\lambda - \lambda_\odot)\cos^2\beta}$$

$$\pm \frac{|\sin(\lambda - \lambda_\odot)|\sqrt{\sin^2\psi - \cos^2(\lambda - \lambda_\odot)\cos^2\beta}}{1 - \cos^2(\lambda - \lambda_\odot)\cos^2\beta}$$

▸ We see that, given a star at a position $(\lambda - \lambda_\odot, \beta)$ relative to the Sun, then for a precession cone angle ψ one can vary the spin phase θ and the precession phase φ until the star is in the field of view of viewport 1 (and likewise for viewport 2). This will in general occur for two values of (θ, φ), with two corresponding values of scan angle q.

▸ For each set of values ψ and $\lambda_\odot$, there will be a region of the sky that is visible, corresponding to a 2π range of the precession and spin phase angles. The boundaries of this allowed region are determined by the locations where the square root term in Q becomes imaginary. **There are two resulting inaccessible "holes" in the Sun and anti-Sun directions**, corresponding to the boundaries of the precession cone. The angular radius of the holes, from simple geometry, is $\frac{\pi}{2} - \psi$, which may also be seen by setting $\lambda = \lambda_\odot$ in $\sin^2\psi - \cos^2(\lambda - \lambda_\odot)\cos^2\beta$ from the square root term, leaving $\frac{\pi}{2} - \beta = \pm\psi$.

▸ Figure 5 shows, on a sinusoidal projection of the sky, the value of the square root term as a function of β and $\Delta\lambda = \lambda - \lambda_\odot$, for $\psi = \frac{\pi}{4}$, and with black representing zero. The red circles are the boundaries of the precession cone holes.

▸ The precession cone holes occupy a solid angle that is a function of the precession cone angle. Consider an infinitesimal solid angle element $d\Omega = \sin u\, du\, d\varphi$, where $u = \frac{\pi}{2} - \psi$ is the polar angle. Integrating over $\varphi = 0..2\pi$ and $u = 0..\frac{\pi}{2} - \psi$, we obtain the solid angle occupied by the two holes,

$$\frac{\Omega_{holes}}{4\pi} = 1 - \sin\psi \tag{1}$$

▸ Figure 6 illustrates the scan angle as a function of ecliptic latitude and difference in ecliptic longitude from that of the Sun, for a precession cone angle of 45 degrees. Again, a sinusoidal map projection in $(\Delta\lambda, \beta)$ is used. The blue and yellow surfaces correspond to the two solutions. The holes due to the precession cone in the Sun and anti-Sun directions, shown in black, are readily apparent.

• The *faux* discontinuities near $\Delta\lambda \simeq \pm130\,\mathrm{deg}$ and $\Delta\lambda \simeq \pm40\,\mathrm{deg}$ are merely due to wrapping of q from -180 to 180 degrees. There are real discontinuities at
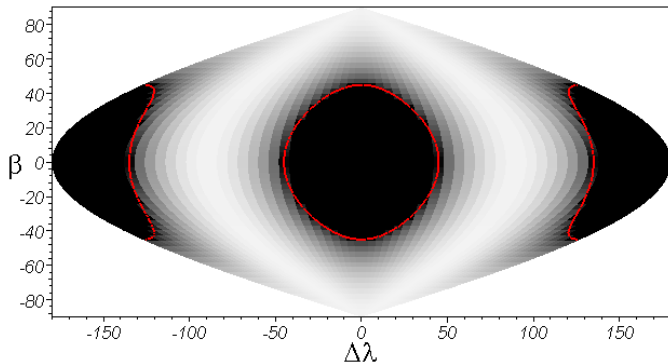

Figure 5 — Square root term of Q as a function of position on the sky relative to the Sun. Black regions correspond to precession cone holes, the boundaries of which are indicated by the red curves. Map projection is a sinusoidal equal-area projection.
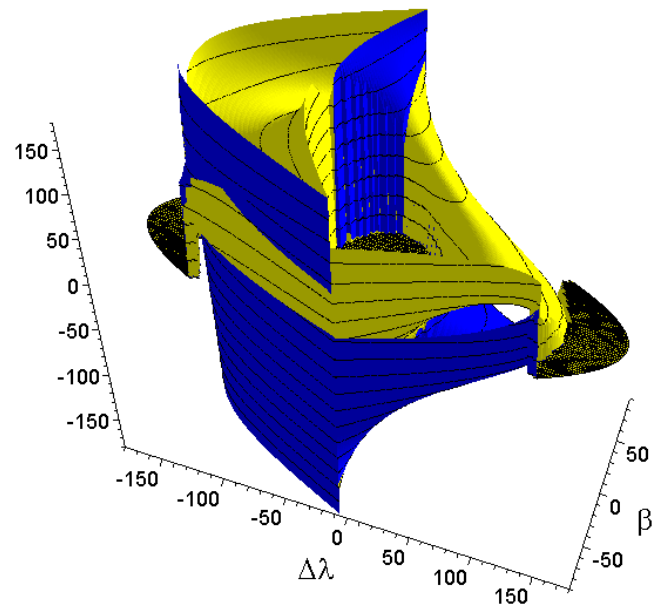

Figure 6 — FAME scan angle as a function of position on the sky relative to the Sun. Map projection is a sinusoidal equal-area projection.

$\Delta\lambda = 0, \pi$. The two solutions become identical at the discontinuities (note in the figure the continuation of contour lines across the discontinuities). Hence, the surfaces match across the discontinuities to produce two continuous smoothly deformed sheets (except precisely at the infinitesimal discontinuities).

- The effect of decreasing the precession cone angle is to increase the radius of the precession cone holes by the same amount and to increase the fraction of the sky covered by the holes

▸ The structure in Figure 6 will **smear in longitude** due to Earth's orbital motion — **but not in latitude**.

4. THE IMPORTANCE OF THE CROSS-SCAN ROTATION RATE

▸ Rotations of the spacecraft result in star motions at the focal plane in the scan and cross-scan directions, as well as in field rotation. The two viewports will see different proportions of these motions, due to their separation by the basic angle γ. By definition, the body y axis pierces the center of the viewport 1 field of view. Hence, for viewport 1 we have $\Omega_x = \Omega_c, \Omega_y = \Omega_r,$ and $\Omega_z = \Omega_s$, where $[\Omega_c, \Omega_r, \Omega_s]$ are the cross-scan, field rotation, and in-scan rotation rates.

▸ Decompose the angular velocity vector along these three axes.

▸ As functions of ecliptic coordinates, these rotation rate components are:

Cross-scan rate:

$$
\begin{aligned}
\Omega_c =\ & \frac{\cos(\lambda - \lambda_\odot)\cos\beta}{\sin\psi}\frac{d}{dt}\psi \\
& + \frac{[Q\cos^2\beta\cos(\lambda - \lambda_\odot)\cos\psi - \sin^2\psi\sin\beta]\sin(\lambda - \lambda_\odot)}{Q\sin\beta - \cos\psi\cos(\lambda - \lambda_\odot)}\frac{d}{dt}\phi \\
& + \left\{ \frac{Q^2\cos^2\psi\cos(\lambda - \lambda_\odot)\sin(\lambda - \lambda_\odot)\cos^3\beta}{\sin^2\psi[Q\sin\beta - \cos\psi\cos(\lambda - \lambda_\odot)]} \right. \\
& \quad - \left[\frac{Q\cos\psi\sin\beta\sin(\lambda - \lambda_\odot)}{Q\sin\beta - \cos\psi\cos(\lambda - \lambda_\odot)} \right. \\
& \quad + \left. \left. \frac{\cos\psi\cos^2(\lambda - \lambda_\odot) - Q\sin\beta\cos(\lambda - \lambda_\odot)}{\sin(\lambda - \lambda_\odot)\sin^2\psi} \right]\cos\beta \right\}\frac{d}{dt}\lambda_\odot
\end{aligned}
$$

Field rotation rate:

$$
\begin{aligned}
\Omega_r =\ & \cos(\lambda - \lambda_\odot)\cos\beta\frac{d\phi}{dt} + \sin\beta\frac{d\lambda_\odot}{dt} \\
& + \frac{[\sin^2\psi\sin\beta - Q\cos^2\beta\cos(\lambda - \lambda_\odot)\cos\psi]\sin(\lambda - \lambda_\odot)}{\sin\psi[Q\sin\beta - \cos\psi\cos(\lambda - \lambda_\odot)]}\frac{d\psi}{dt}
\end{aligned}
$$

In-scan rate:

$$
\Omega_s = \frac{d\theta}{dt} + \frac{d\phi}{dt}\cos\psi - Q\cos\beta\frac{d\lambda_\odot}{dt}
$$

▸ Figure 7 shows the field rotation rate (the signal is dominated by the precession term). The specific case of FAME is used for illustration.

▸ Figure 8 shows the cross-scan rotation rate (the signal is again dominated by the precession term) for the same numerical case.

▸ **The cross-scan rate determines the density of observations on the sky.** From Figure 8:

- Expect a pile-up of density near the precession cone hole boundaries (cross-scan rate approaches zero).

- The structure shown will smear in longitude due to Earth's orbital motion.

- There are two zones in latitude where the density is maximum. There will be a depression of mean astrometric errors in these zones.
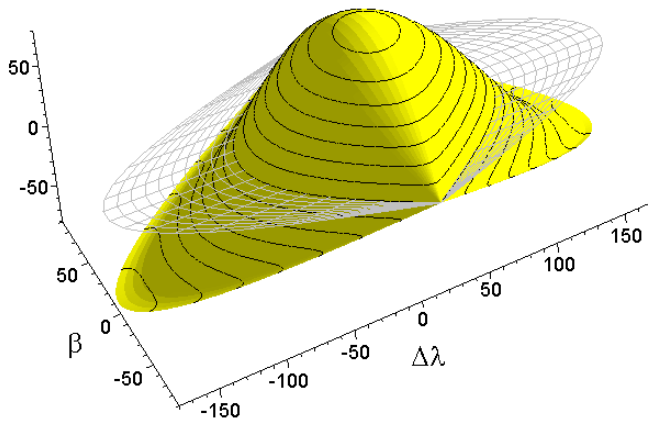

Figure 7 — FAME field rotation rate due to precession, in units of hundredths of arc seconds per second, as a function of position on the sky relative to the Sun. Map projection is a sinusoidal equal-area projection.
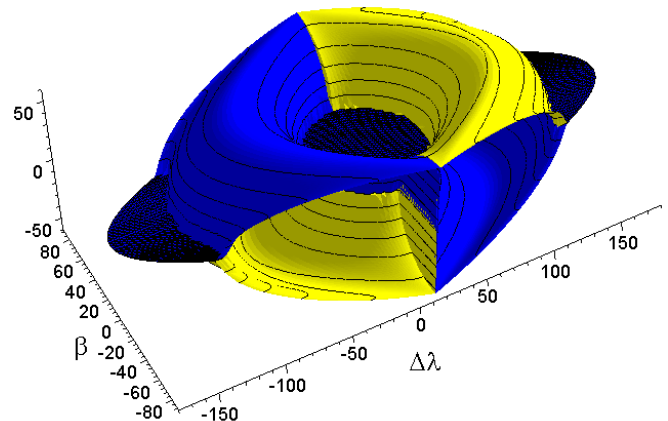

Figure 8 — FAME cross-scan rotation rate due to precession, in units of hundredths of arc seconds per second, as a function of position on the sky relative to the Sun. Map projection is a sinusoidal equal-area projection.
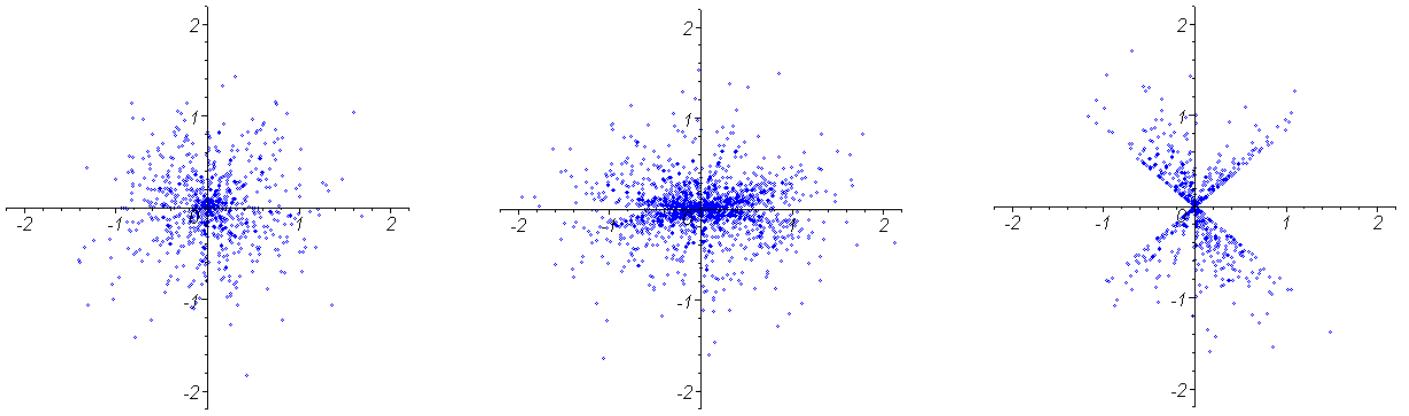
Figure 9 — Scatter plots of observations selected from three representative locations on the sky. Left: high ecliptic latitude. Center: mid-latitude. Right: low latitude. Plot scale is milliarcseconds.

- The high-density zones move to higher latitude with smaller Sun angle.

▶ **We are now in a position to simulate observations and understand the geometric causes of the results.**

5. SIMULATION DETAILS

▶ Observations with single-measurement errors drawn from a distribution were accumulated on an equal-area grid on the sky as the spacecraft was allowed to spin and precess. Nominal FAME values were adopted.

▶ 1-σ scan-direction single-measurement error = 580 µas. This sets the units for the results: µas for parallax and position, and µas/yr for proper motions. Sampled from Gaussian error distribution.

▶ grid = [341,171], evenly spaced in [longitude, sin latitude]

▶ Δt = amount of time to scan across one grid cell at equator in longitude direction

- determined by the grid size specification and the spin period

▶ spin periods: 35, 40, and 45 minutes

▶ precession periods: 15, 20, and 30 days

▶ precession cone angles: 35, 40, and 45 deg

▶ simulation times: 2.5 years (nominal) and 5 years (extended)

▶ 2 viewports (telescopes)

▶ basic angle = 81.5 deg

▶ Observations were performed by between 1 and 4 detectors per viewport passage. The number of detectors corresponds to the number of astrometric CCDs in one of the 9 CCD columns on the focal plane. The column was chosen randomly for each focal plane crossing of a grid cell.

▶ astrometric CCD count by column: 123242321 (nominal FAME configuration).

▶ An option for calculating normal points was available for multiple CCD encounters per focal plane crossing.

▶ Least squares solutions for the astrometric parameters and their errors were performed for each grid cell.

▶ Sun-tracking variation of Sun angle (~4°) not included.

6. SIMULATION RESULTS

6.1. Scan Angle Distribution Snapshots

▶ The observations shown in Figure 9 illustrate the distributions of scan angle from representative locations on the sky (plot scale is milliarcseconds).

- At high ecliptic latitude, the scan angle distribution is uniform, which will lead to better astrometric accuracies.

- At lower latitudes, the scan angle distribution becomes nonuniform.

- The limiting case is at the ecliptic. The cone angle is determined by the precession cone angle.

6.2. Observation Geometry and Least Squares

Refer to Figure 10. The instrument makes an observation of a star, deriving ΔS and ΔC (scan and cross-scan positions) with respect to local ecliptic coordinates [$\Delta\lambda, \Delta\beta$] located on the sky at [$\lambda_{ref}, \beta_{ref}$]. Scan direction is indicated, making an angle q wrt the local ecliptic meridian ($\Delta\beta$ axis). The observation point is not coincident with the star due to single-measurement errors.

Measurement errors are in general orders of magnitude worse cross-scan than in-scan, causing the measurement error ellipse to be extremely elongated. We therefore approximate it as the limiting case: an "observation line". (Note that ΔC is not drawn to scale in the figure.) Given a number of observations, the distance y of the observation lines from the true location of the star then becomes the most natural quantity to minimize in a least squares sense.

Due to Earth's orbital motion, the star moves on an ellipse on the sky, with semimajor axis a and eccentricity $\cos\beta$. Due to proper motion [μ_λ, μ_β], the center of the ellipse moves during the mission. The least squares algorithm minimizes the length of the perpendicular line segment y by solving for the
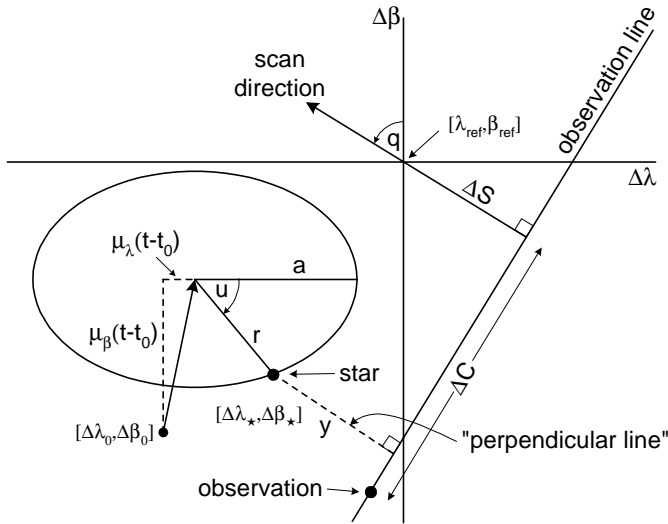
Figure 10 — Observation geometry used to estimate astrometric parameters via linear least squares.

astrometric parameters: (1) the position $[\Delta\lambda_0, \Delta\beta_0]$ of the ellipse center at epoch t_0, (2) the proper motion components $[\mu_\lambda, \mu_\beta]$, and (3) the semimajor axis a of the parallactic ellipse. The resulting covariance matrix then yields the formal errors and cross-correlations of the parameters.

The perpendicular distance is

$$|y| \simeq | \Delta S$$
$$- a\left[\sin(\lambda_{ref} - \lambda_\odot)\sin q + \sin\beta_{ref}\cos(\lambda_{ref} - \lambda_\odot)\cos q\right]$$
$$+ \left[\Delta\beta_0 + (t - t_0)\mu_\beta\right]\cos q - \left[\Delta\lambda_0 + (t - t_0)\mu_\lambda\right]\sin q \ |$$

6.3. General Characteristics of the Two Distributions

▸ Observation density distribution (Figure 11)

- Highest density at top & bottom of precession cone holes (which smear in longitude), corresponding to two zones in latitude $|\beta| = \frac{\pi}{2} - \psi$.

- Lowest densities are in ecliptic band between the high-density zones.

- Ecliptic band exhibits density "ribbing" corresponding to the times when the spacecraft spin axis lies in ecliptic plane.

  ⇨ Best accuracies should be in the mid-latitude high-density zones.

  ⇨ Worst accuracies should be in the ecliptic band.

  ⇨ Ecliptic band is not uniformly bad.

▸ Scan angle distribution

- Homogeneous in polar cap regions (latitudes above high-density zones)

- Cone-shaped on ecliptic, with cone opening angle $\frac{\pi}{2} - \psi$.

  ⇨ Better position accuracies in polar cap regions.

  ⇨ Longitude position accuracy substantially degraded near ecliptic.
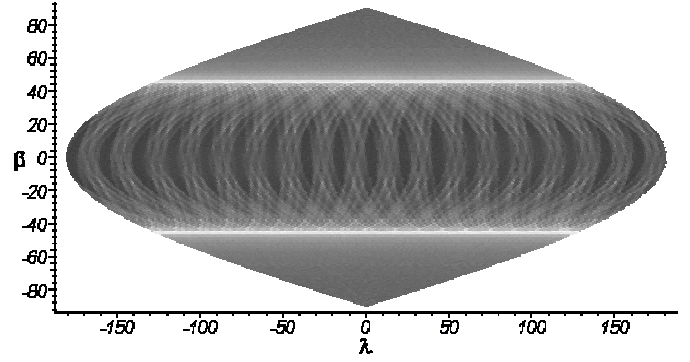
Figure 11 — Observation density (nominal FAME mission) as a function of ecliptic coordinates. Note (1) the mid-latitude high-density zones, as well as (2) the low-latitude "ribbing" and (3) the uniformity at high latitudes. Map projection is a sinusoidal equal-area projection.
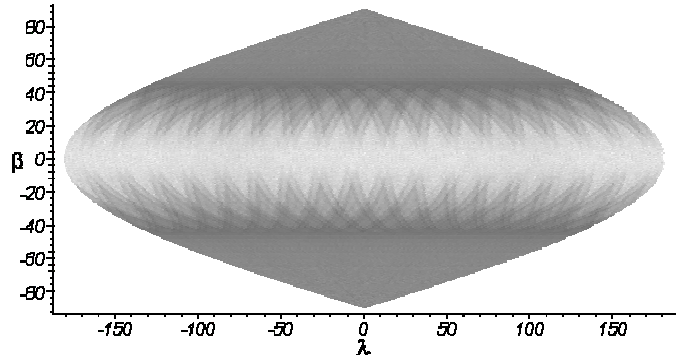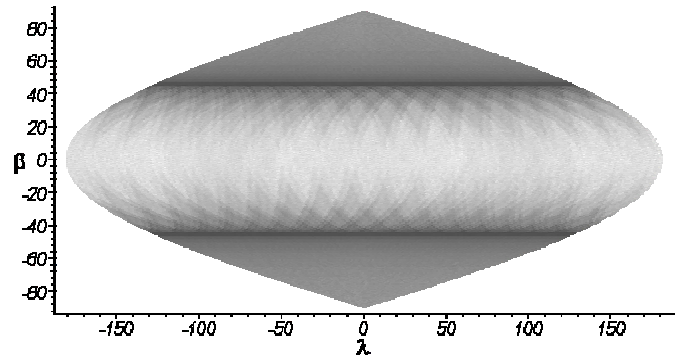

Figure 12 — Parallax errors (log scaling).
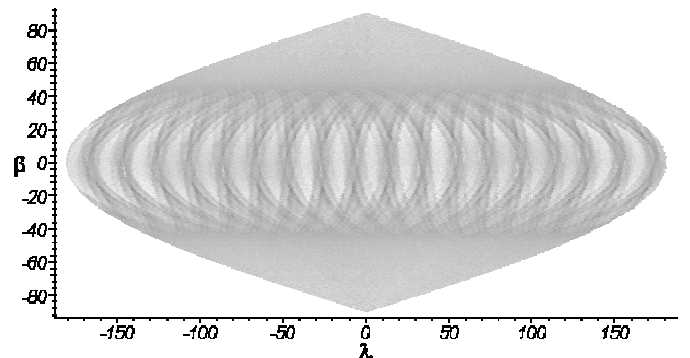

Figure 13 — Longitude errors (linear scaling).

Figure 14 — Latitude errors (linear scaling).

⇨ Latitude position accuracy slightly degraded near ecliptic.

⇨ Better parallax accuracy in polar cap regions.

6.4. Error Distributions on the Sky

▶ The structure of the mission-averaged astrometric error distributions is similar to that of the observation density distribution. See Figures 12-14.

6.5. Histogram Components and Behavior

▶ See Figure 15.

▶ sky naturally divided by scanning geometry into distinct regions:

- high-density troughs at $|\beta| = \frac{\pi}{2} - \psi$
- ecliptic band $|\beta| < \frac{\pi}{2} - \psi$
- polar caps $|\beta| > \frac{\pi}{2} - \psi$

▶ as Sun angle decreases:

- polar caps shrink
- ecliptic band grows
- longitude
  - ◆ high-accuracy population shrinks, moves left
  - ◆ low-accuracy population grows, moves right
- latitude
  - ◆ distribution broadens and peak moves left
- parallax
  - ◆ main feature shrinks, moves left
  - ◆ poor-accuracy fraction grows

6.6. Variation of Precession Cone Angle

▶ Three cases were run with precession cone angles (i.e., nominal Sun angles) of 35, 40, and 45 degrees. See Figures 16-28.

▶ Larger than 45 degrees runs into trouble with shield size (hardware complexity and cost, in addition to increase of perturbations). Smaller than 35 degrees and we won't meet the mission requirements.

▶ In general, the mission astrometric errors degrade as the nominal Sun angle decreases.

▶ We do very well in latitude errors: histogram peaks are around 26-28 μas, and 100 percent of the sky is better than 37 μas even for the worst case. Hence, with respect to latitude errors, mission requirements are not affected by nominal Sun angle in the range 35-45 degrees.

▶ Nearly 100 percent of the sky is 50 μas or better in both longitude (99.99%) and parallax (98.1%) for the 45 degree case. Going to 40 degrees costs us about 18 percent of the sky at 50 μas in parallax, and it costs about 14 percent of the sky at 50 μas in position in longitude. At 35 degrees
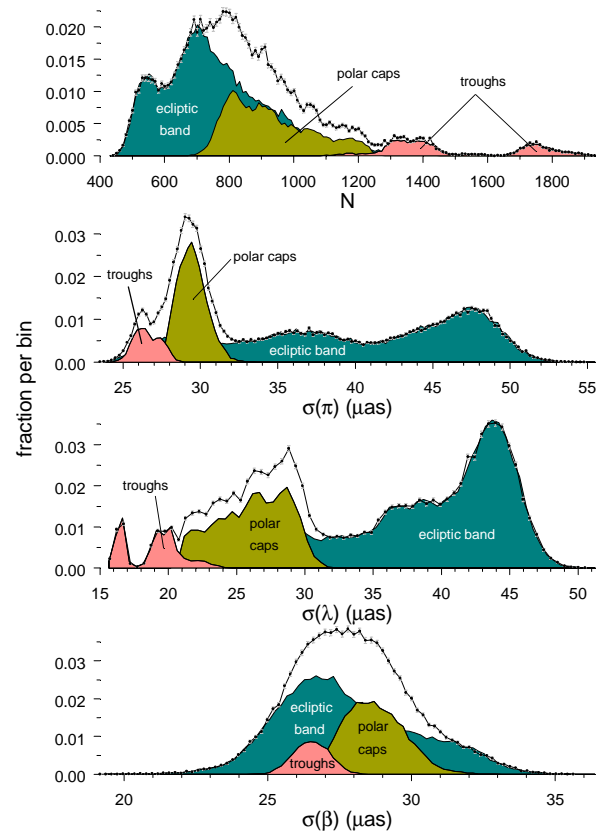

Figure 15 — Histograms of the observation density, parallax, and position distributions, showing components from three regions on the sky.

nominal Sun angle the requirement of 90 percent of the sky at 50 μas or better is not met.

▶ However, even at 35 degrees, the worst parallax error is only 69 μas and the worst longitude error is only 67 μas.

▶ Proper motion in longitude significantly fails the 90 percent of the sky, <50 μas/yr target for all three precession cone angles.

▶ The parallax requirement of 90 percent of the sky better than 50 μas restricts the precession cone angle to greater than or equal to 43 degrees.

▶ Ratios of errors in the ecliptic region to those in the polar regions get substantially worse for longitude and parallax as you decrease the nominal Sun angle from 45 degrees to 35 degrees (see the plot of median values by latitude, shown in Figure 28). The corresponding ratios get slightly better for errors in latitude, but the difference is so small as to not matter.

▶ The observation count is roughly in the range 600-1000 for most areas of the sky. The dominant histogram peak shifts towards lower counts as the precession cone angle decreases.

▶ A test was run during which normal points were simulated whenever more than one CCD was encountered during a focal plane crossing. In such cases, the weight of the observation was proportional to the number of CCDs in the given
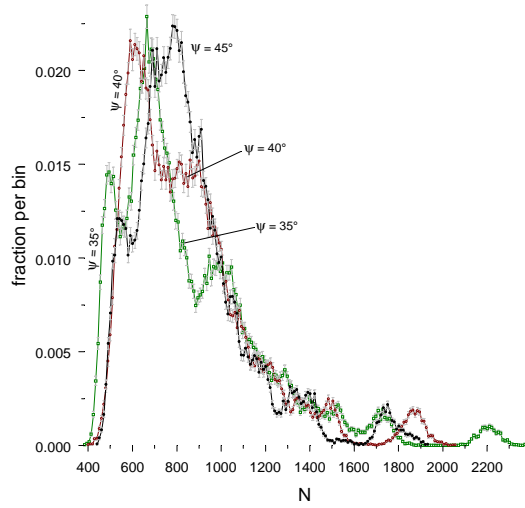
Figure 16 — Histograms of observation counts (fraction in each bin). Error bars are 1 σ, assuming Poisson statistics for each bin.
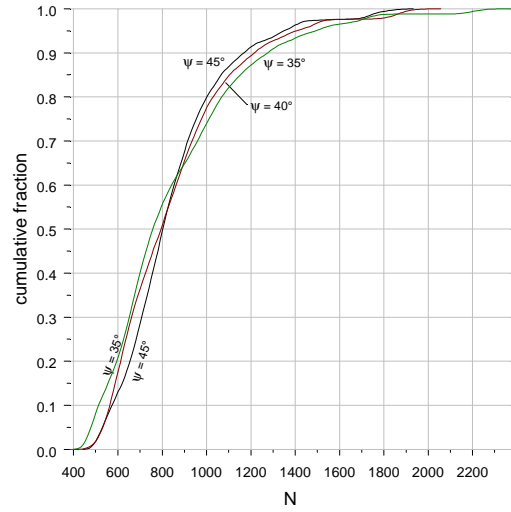

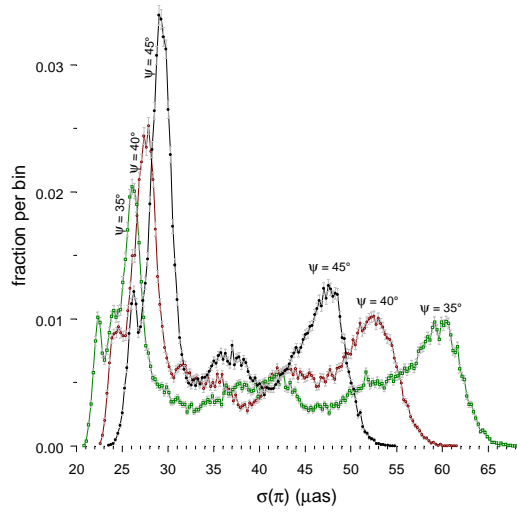Figure 17 — Cumulative histograms of observation counts.

Figure 18 — Histograms of parallax errors.
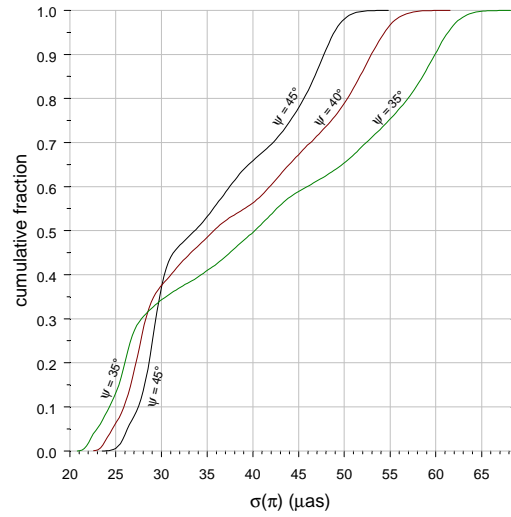

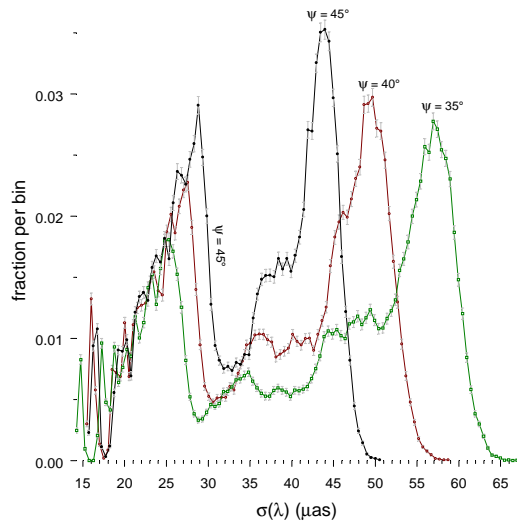Figure 19 — Cumulative histograms of parallax errors.

Figure 20 — Histograms of longitude errors.
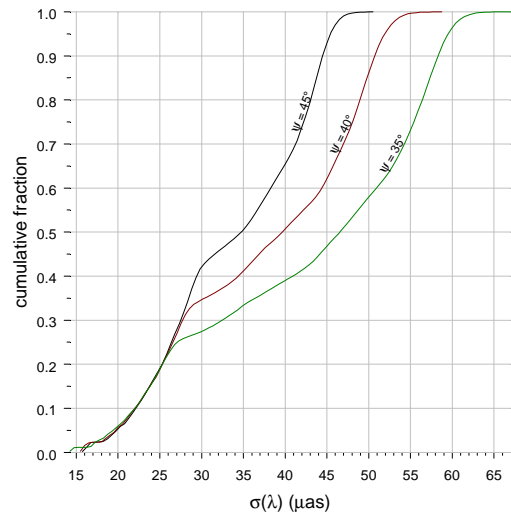

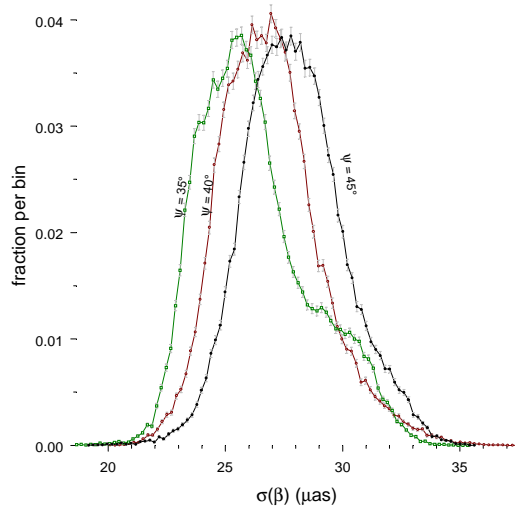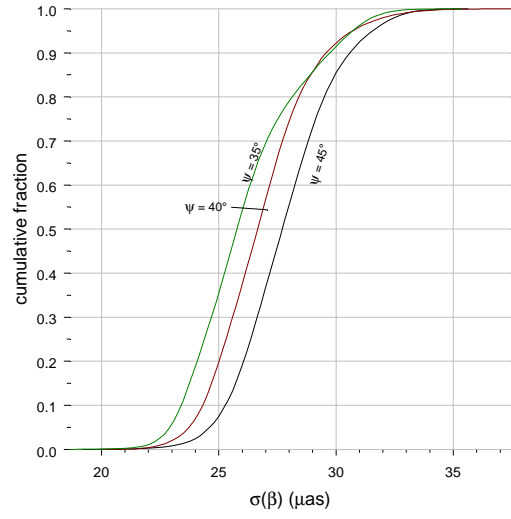Figure 21 — Cumulative histograms of longitude errors.

Figure 22 — Histograms of latitude errors (fraction in each bin). Error bars are 1 σ, assuming Poisson statistics for each bin.

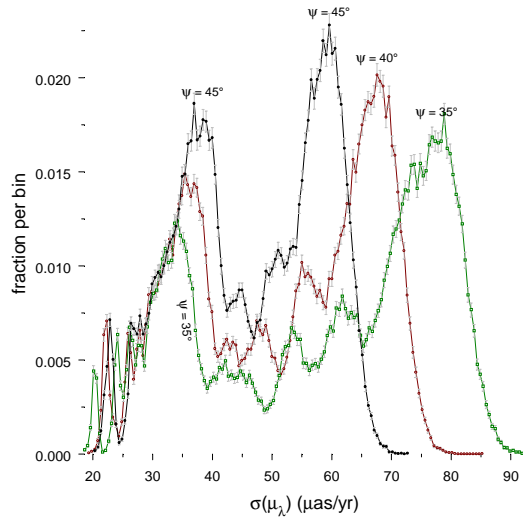Figure 23 — Cumulative histograms of latitude errors.

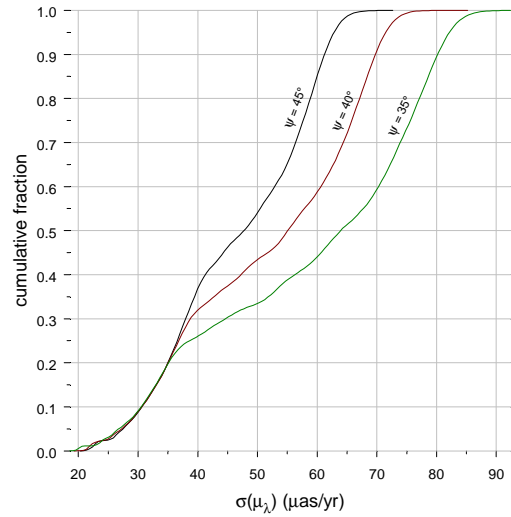Figure 24 — Histograms of longitude proper motion errors.

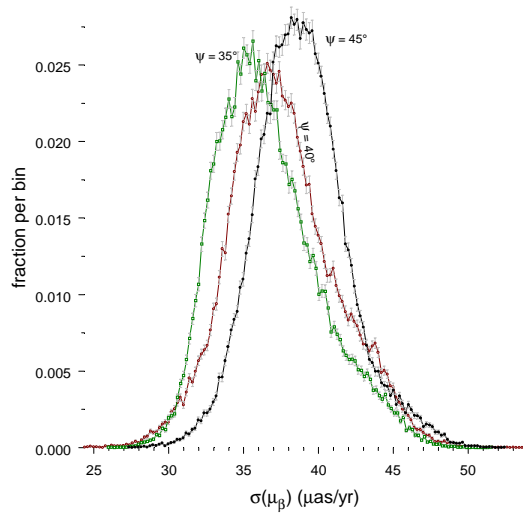Figure 25 — Cumulative histograms of longitude pm errors.

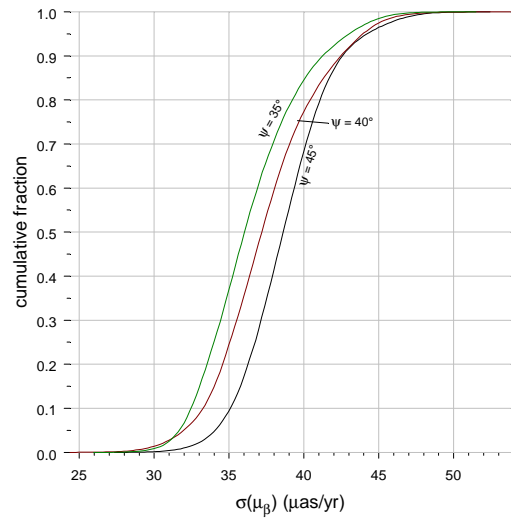Figure 26 — Histograms of latitude proper motion errors.

Figure 27 — Cumulative histograms of latitude pm errors.

column. There was almost no difference in the resulting astrometric error distributions.

▸ Table 1 shows percentages of the sky for which a 2.5 year FAME mission can meet or do better than the goals of 50 μas (position, parallax) and 50 μas/yr (proper motion), for three nominal Sun angles and assuming a 580 μas single-measurement standard error.

Table 1

	45 deg	40 deg	35 deg
parallax	98	79	65
longitude	100	86	58
latitude	100	100	100
pm-longitude	54	43	33
pm-latitude	100	100	100

▸ Table 2 shows minimum, median, average, and maximum values from the simulations. Units are μas and μas/yr.

6.7. Variation of Spin Period

▸ Three cases were run with spin periods of 35, 40, and 45 minutes. See Figures 29-31 (left column of next page).

▸ There is almost no discernible difference in the structure of the observation density distribution as the spin period changes, at least in the range 35 to 45 minutes. The density scales uniformly as a function of the spin period.

▸ In general, the mission astrometric errors degrade as the spin period increases.

▸ Proper motion in longitude significantly fails the 90 percent of the sky, <50 μas/yr target for all three spin periods.

▸ The parallax requirement of 90 percent of the sky better than 50 μas restricts the spin period to less than or equal to 43 minutes.

▸ Table 3 shows percentages of the sky for which a 2.5 year FAME mission can meet or do better than the goals of 50 μas (position, parallax) and 50 μas/yr (proper motion), for three spin periods (35, 40, and 45 minutes), nominal Sun angle of 45 degrees, and assuming a 580 μas single-measurement standard error.

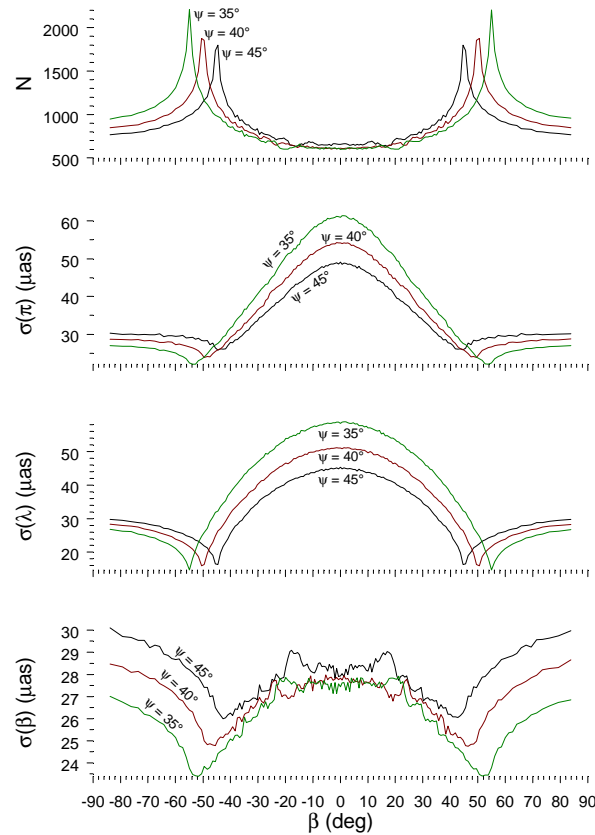Figure 28 —Medians of longitude bands as a function of ecliptic latitude.

Table 3

	35 min	40 min	45 min
parallax	100	98	86
longitude	100	100	98
latitude	100	100	100
pm-longitude	62	54	48
pm-latitude	100	100	98

Table 2

|	45 degrees				40 degrees				35 degrees			
	min	med	avg	max	min	med	avg	max	min	med	avg	max
counts	430	808	854	1,959	370	799	854	2,054	392	762	854	2,362
parallax	23.4	33.8	36.1	55	22.4	35.9	38.1	61.4	20.7	40.3	41.1	68.5
longitude	15.4	35	34	51.5	15.3	39.9	37.8	60	14.1	46.8	42.8	67.1
latitude	19.1	27.8	27.9	37.8	20.1	26.8	26.9	37.7	18.6	25.9	26.2	35.2
pm-longitude	20	47.9	46.9	73.2	19.1	55.4	52	82	18.4	64.2	58.9	94.1
pm-latitude	27.5	38.7	38.9	53.6	24.3	37.3	37.6	53	25.6	36.1	36.6	51.1
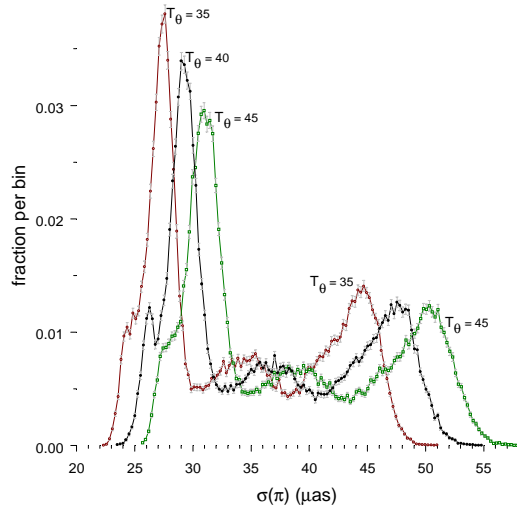
Figure 29 — Histograms of parallax errors (fraction in each bin). Error bars are 1 σ, assuming Poisson statistics for each bin.
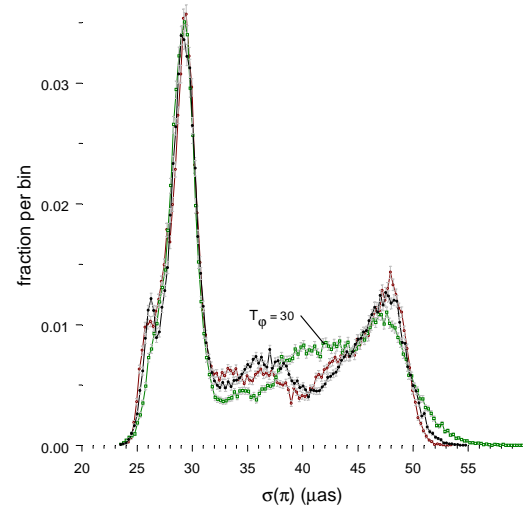

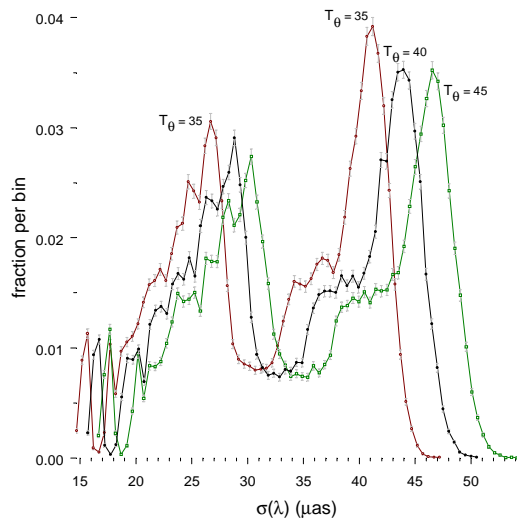Figure 32 — Histograms of parallax errors.
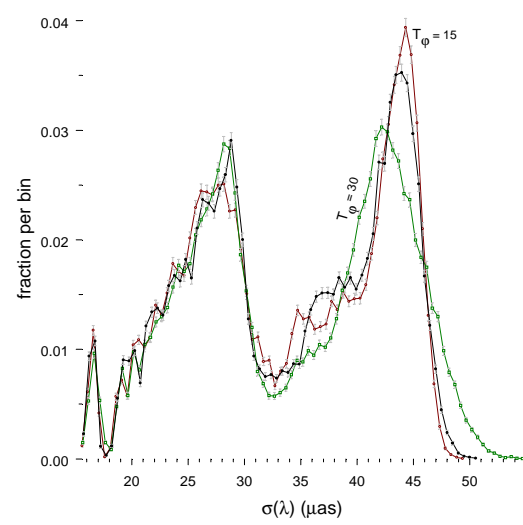

Figure 30 — Histograms of longitude errors.

Figure 33 — Histograms of longitude errors.

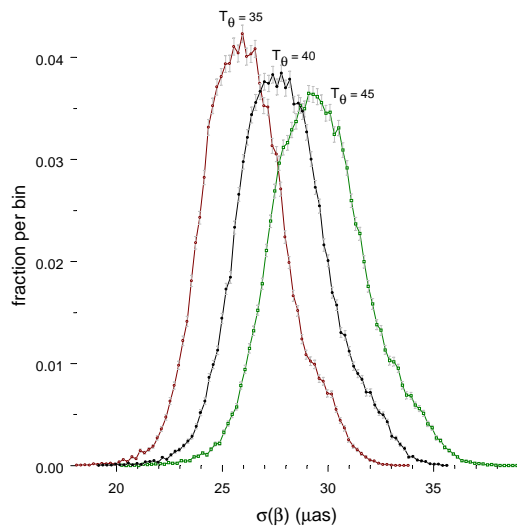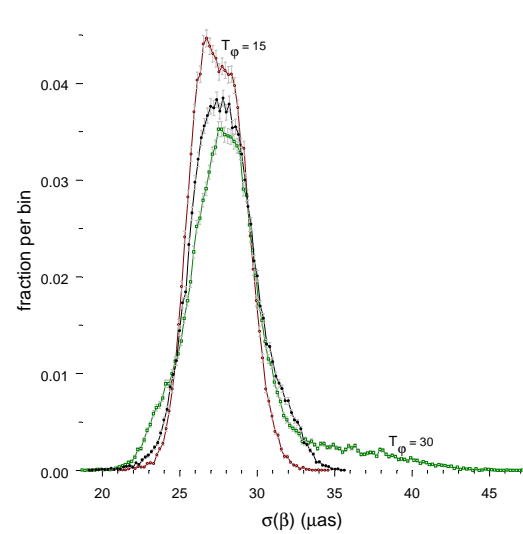Figure 31 — Histograms of latitude errors.

Figure 34 — Histograms of latitude errors.

Table 4

	35 minutes				40 minutes				45 minutes			
	min	med	avg	max	min	med	avg	max	min	med	avg	max
counts	505	924	977	2,226	430	808	854	1,959	377	718	760	1,750
parallax	22.4	31.6	33.8	50.8	23.4	33.8	36.1	55	25.6	35.9	38.3	58
longitude	14.5	32.7	31.8	47.4	15.4	35	34	51.5	16.4	37.1	36.1	54.4
latitude	17.9	26	26.1	33.2	19.1	27.8	27.9	37.8	20.2	29.5	29.6	39
pm-longitude	18.9	44.9	43.8	67.6	20	47.9	46.9	73.2	21.2	50.9	49.8	76.8
pm-latitude	26	36.2	36.3	48.9	27.5	38.7	38.9	53.6	28.9	41.1	41.3	55.6

▸ Table 4 shows minimum, median, average, and maximum values for spin periods of 35, 40, and 45 minutes. Units are μas and μas/yr. Precession cone angle is 45 degrees.

6.8. Variation of Precession Period

▸ Three cases were run with precession periods of 15, 20, and 30 days. See Figures 32-34 (right column of previous page).

▸ The structure of the observation density distribution on the sky is sensitive to the precession period. Coverage is more uniform for smaller precession periods.

▸ However, there is almost no difference in the mission astrometric errors for precession periods in the range 15 to 30 days.

▸ Results begin to deteriorate around 30 days, which therefore probably represents a reasonable upper bound on the precession period.

6.9. A 5-Year Extended Mission

▸ The nominal mission was run but with an extended mission length of 5 years. See Figures 35-38.

▸ The observation density is smoother — longitudinal ribbing effect is lessened (compare the observation density all-sky image of the 2.5-year case to that of the 5-year case).

▸ All errors fall well within the 50 μas or μas/yr mission requirements.

▸ Position in latitude and both proper motion components are entirely less than 25 μas or μas/yr.

▸ The polar cap parallax feature is at about 21 μas.

▸ Results from a 5-year mission (45 degrees) are shown in Table 5. They agree with the expected $t^{-1/2}$ dependence for position and parallax and $t^{-3/2}$ for proper motion.

Table 5

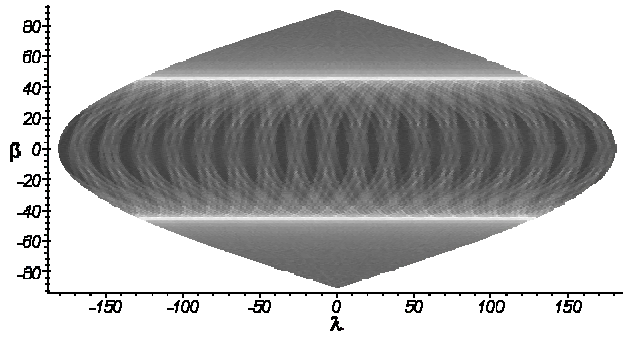|	min	med	avg	max
counts	1,009	1,600	1,709	3,797
parallax	16.5	23.2	25.2	37.2
longitude	11	23.7	23.5	33.6
latitude	15.2	19.2	19.2	22.5
pm-longitude	7.3	17.1	16.5	24.5
pm-latitude	9	13.6	13.5	17.2

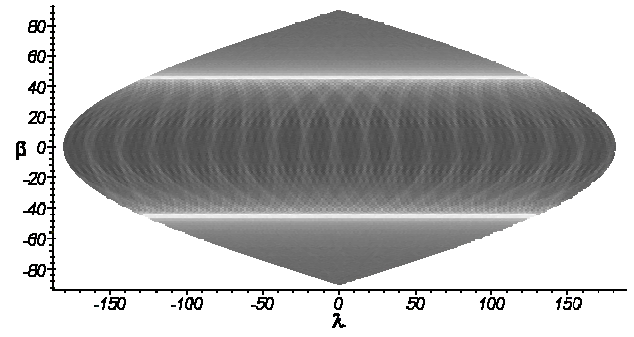Figure 35 — Observation density of a 2.5 year mission.

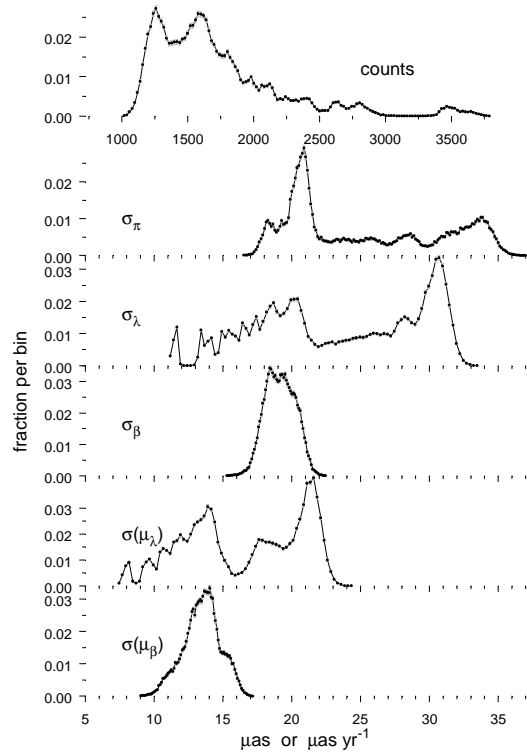Figure 36 — Observation density of a 5 year mission.
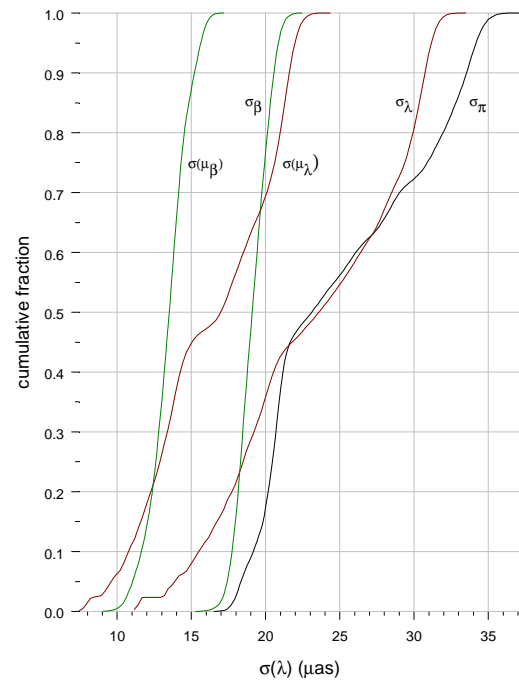

Figure 37 — Histograms for a 5 year mission.

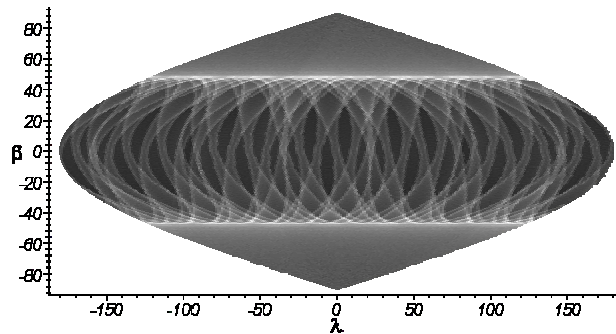Figure 38 — Cumulative histograms for a 5 year mission.

Figure 39 — Observation density of the Hipparcos mission (for fun).